RAA 2021 Vol. **21** No. **7**, 156(8pp) doi:10.1088/1674-4527/21/7/156

http://www.raa-journal.org *http://iopscience.iop.org/raa*

Research in Astronomy and Astrophysics

A preliminary study on photogrammetry for the FAST main reflector measurement

Wei-Min Li* and Liu-Jian Zhou

Department of Precision Machinery and Precision Instrumentation, University of Science and Technology of China, Hefei 230026, China; *liwm@ustc.edu.cn*

Received 2020 November 27; accepted 2021 January 25

Abstract The Five-hundred-meter Aperture Spherical radio Telescope (FAST) is the largest single-dish radio telescope in the world. In this paper, we apply photogrammetry to measure local area surface accuracy of the FAST main reflector. Contrast with the existing photogrammetric methods that need to stick the cooperation target on the panel. In this paper, we directly detect nodes according to their natural feature. Analyzing the FAST reflector composition, we propose a two-step Hough transform method for node detection. Due to the high similarity of the neighboring area around nodes, it is hard to match two images by the feature matching method. Therefore, we apply the nodes combination approach to obtain the homography matrix between two photos for nodes matching. After nodes detection and matching, triangulation and bundle adjustment algorithms are adopted for 3D reconstruction. During the experiment, the adjusted node position deform a local area of the FAST main reflector into a spherical cap with a radius of 300 m. The experimental result shows that the measurement accuracy of the sphere with a radius of 300 m is 12.299 mm, indicating that it is feasible to apply photogrammetry for the FAST main reflector measurement.

Key words: FAST — photogrammetry — node detection — bundle adjustment — 3D reconstruction

1 INTRODUCTION

The Five-hundred-meter Aperture Spherical radio Telescope (FAST), built on the unique karst landscape in Guizhou Province, completed and put into use in 2016, is a Chinese mega-science project and the largest single dish radio telescope in the world (Nan 2006; Li & Pan 2016).

FAST includes a spherical cap-shaped active reflector with a diameter of 500 m. It consists of 4450 triangular unit panels, and there are 6670 steel cables to form cable-net support them. The triangular unit panels with a side length of 11 m are connected by approximately 2250 nodes, and each node corresponds to a driving cable down-tied to an actuator on the ground (Nan & Li 2014; Tang et al. 2020). During an observation, by adjusting the driving cable, the reflector will deform into a paraboloid with a diameter of 300 m.

The active reflector surface accuracy is a crucial indicator of the radio telescope, which determines the antenna efficiency and the shortest observable wavelength (Ruze 1966). Surface shape measurement is a fundamental technology for astronomical telescopes. The original surface shape measurement technology is through the theodolite with two degrees of freedom and its improved method, such as the Lovell 76 m radio telescope in Britain (Morison 2007) and the Effelsberg 100 m radio telescope in Germany (Wielebinski et al. 2011). The Greenbank 100 m radio telescope in the United States began to apply laser measurement technology (Hall et al. 1998). For the method mentioned above, measuring speed is slow and inflexible.

Nowadays, photogrammetry technology is widely used in surface shape measurement (Subrahmanyan 2005; Edmundson & Baker 2001) due to its advantages of non-contact, long-distance, fast speed, and high precision. The Arecibo 305 m radio telescope has improved its surface accuracy from 15 mm to about 5 mm by using the photogrammetric method (Edmundson & Baker 2001). In their scheme, approximately 2000 retro-reflective targets were placed on the primary reflector surface, primarily at locations where tieback cables attach to the main cable support grid. It takes a lot of staff and time to place targets. Since the retro-reflective targets are used, the image needs to be captured when the sun drops to the point where there is no direct sunlight hitting the surface of the main

* Corresponding author

reflecting surface, which is greatly affected by the weather. In reference (Zhou et al. 2010), they measure the single triangular unit panel by photogrammetry. Similarly they set the target object for measurement and the accuracy is 3 mm.

The traditional photogrammetry method needs to stick the cooperative target on the reflector and without its deformation. For the FAST requirement, it is hard to paste the cooperative target due to the reflector deformation during observation. To settle this problem, we detect the node by its natural feature as image information. In this paper, we use the photogrammetric method to measure a local area of the FAST main reflector, laying the foundation for the entire reflector measurement.

2 NODE DETECTION

When the photogrammetry is applied to measure the main reflector surface shape, one or more cameras shoot it from different directions to collect its images, as shown in Figure 1(a). The fundamental step of photogrammetry is to extract the target feature information such as characteristic points or characteristic lines through digital image processing technology in the captured images. According to the FAST main reflector composition, a two-step method is adopted to detect nodes, the first step is to locate the approximate position of the nodes in the image, and the second step is to obtain the region of interest (ROI) for precise positioning of the nodes.

2.1 Rough Detection

There are splicing gaps between adjacent triangular unit panels on the main reflector, as shown in Figure 1(b). The gray level of the splicing gap and the reflector have distinct contrast, roughly the former occupies the same proportion in different images. According to this feature, perform antilog transformation on the image and set a threshold in the grayscale statistical histogram of the obtained image to binarize it, as shown in Figure 2(a). Use the canny algorithm (Canny 1986) for edge detection of the binary image and filter noise by connected domain size, the result as shown in Figure 2(b).

The FAST main reflector has a large diameter, the splicing gaps can be regarded as lines in a local area. Since the splicing gaps are wider than the 1-pixel width in images, two lines can be detected after edge detection, as shown in Figure 2(c). Among the existing line detection methods, the Hough transform is applied widely because of its robustness. Hough transform utilizes a voting mechanism to detect not only continuous lines but also broken lines. However, the traditional Hough transform has the disadvantage of large space and long time. Scholars have proposed a series of optimization algorithms (KaLviainen & Hirvonen 1997; Ching 2001; Xu et al. 1990).

Analyzing the FAST main reflector image, the lines obtained after edge detection are mainly distributed in three directions. A two-step line detection method is proposed. The first step is to collect slope information of the lines and obtain the slopes in three main directions. The second step is to obtain the remain parameters of the line by accumulating the value of ρ for each direction, where ρ represents the distance from image origin to the line and the range is $[-d, d]$, $d = \sqrt{w^2 + h^2}$, w is image width and h is image height .

For any two edge points $(x_1, y_1), (x_2, y_2)$ calculate the inclination angle of a line:

$$\theta = \begin{cases} \arctan(\dfrac{y_1 - y_2}{x_1 - x_2}) & x_1 \neq x_2 \\ 90^\circ & x_1 = x_2 \end{cases} \tag{1}$$

For an edge point $P(x_1, y_1)$, select an edge point $Q(x_2, y_2)$ that satisfies Equation (2) calculate Equation (1) to get θ, $\theta \in (-90^\circ, 90^\circ]$.

$$\sqrt{(x_1 - x_2)^2 + (y_1 - y_2)^2} > T \tag{2}$$

T is a threshold and calculation efficiency can be improved by choosing T. Recover the three main directions of the line by accumulating the value of θ. Angle cumulative result as shown in Figure 3(a). The three main directions of the line can be obtained by extracting the three peaks.

For a direction θ, another parameter ρ needs to be determined. For an edge point (x, y), compute Equation (3):

$$\rho = x\cos\theta + y\sin\theta \tag{3}$$

to get ρ. ρ cumulative result in a single direction as shown in Figure 3(b). All parameters of the line (ρ, θ) can be obtained by extracting the peaks. It is noted that there are two lines around each cumulative peak. The rough detection is only to locate the approximate position of the node, so one line can be discarded.

Suppose n lines are detected, parameters are $(\rho_1, \theta_1), (\rho_2, \theta_2), \cdots, (\rho_n, \theta_n)$ respectively. The intersection of two lines $(\rho_1, \theta_1), (\rho_2, \theta_2)$ can be obtained by Equation (4):

$$\begin{cases} x = \dfrac{\rho_1 \sin\theta_2 - \rho_2 \sin\theta_1}{\sin(\theta_2 - \theta_1)} \\ y = \dfrac{\rho_2 \cos\theta_1 - \rho_1 \cos\theta_2}{\sin(\theta_2 - \theta_1)} \end{cases} \tag{4}$$

The lines have multiple intersections near the nodes. Inspired by the clustering method, the closed intersections are merged according to certain criteria such as the closest Euclidean distance, and the rough position of the node is finally determined. The rough detection result as shown in Figure 4.

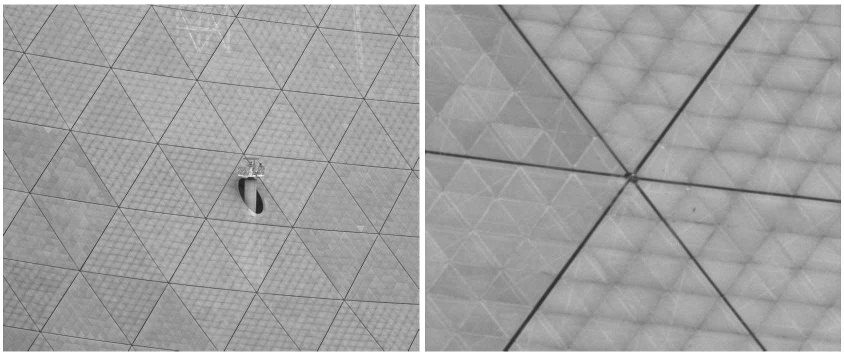

(a) (b)

Fig. 1 Image of the FAST main reflector. (a) Original image. (b) A partial enlarged view.

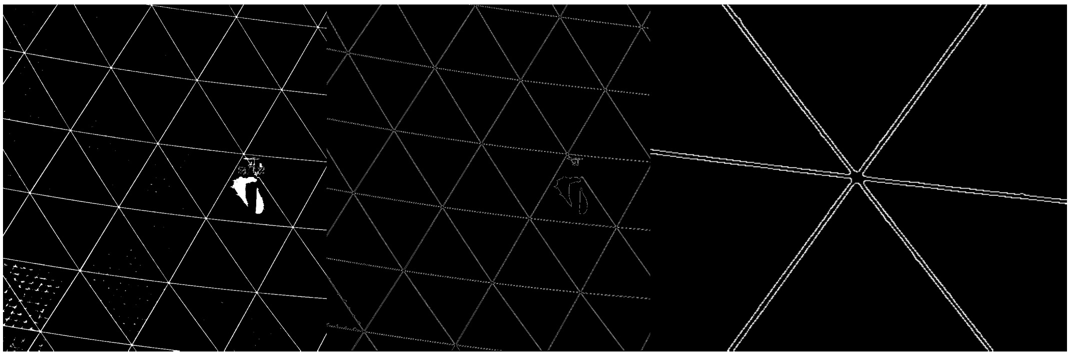

(a) (b) (c)

Fig. 2 (a) Binary image. (b) Edge image. (c) A local area of (b).

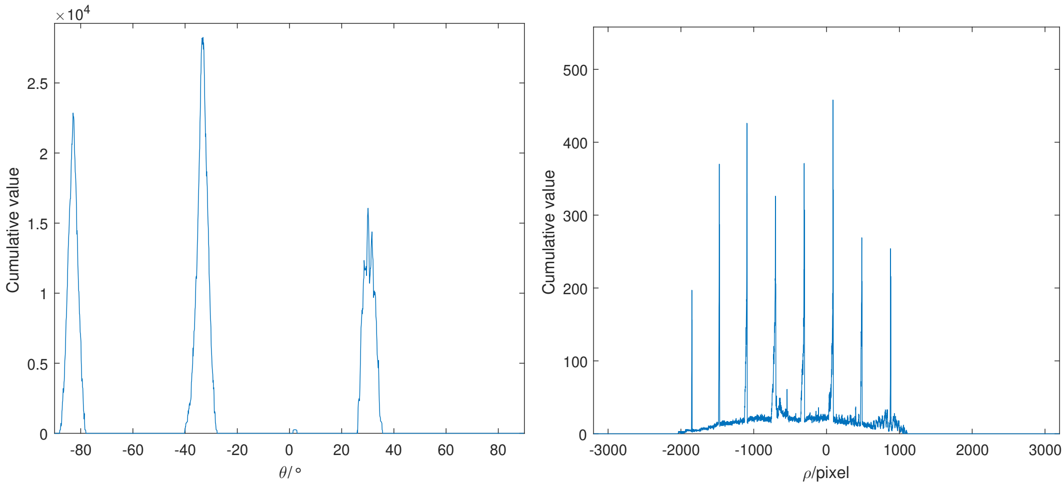

(a) (b)

Fig. 3 Two step Hough transform. (a) θ accumulation result. (b) ρ accumulation result in a single direction.

2.2 Precise Detection

Since the FAST main reflector is a spherical surface, projection to the image plane is a curve. When the field of view is broad enough, rough detection will cause large errors, so it can only give the approximate position of the nodes. For a point, $P(x, y)$, that is roughly detected, the real node position is in a small area near point P, crop a window with certain size around P as an ROI, and perform precise node detection in ROI. The ROI size is determined according to the camera's field of view, a random ROI as shown in Figure 5(a). Perform line Hough transform on ROI, the line detection result as shown in Figure 5(b).

Merge lines according to inclination angle and find the intersection of the lines to complete ROI node detection, the result as shown in Figure 5(c), and the node is marked by red circle. Perform the above operations on each ROI to accomplish all nodes precise detection.

3 NODE MATCHING

Once we have extracted nodes from two or more images, the next step is to establish node matches between these images. Traditional matching methods use the area around the node to generate feature descriptors, and perform matching process through the Euclidean distance of the feature vector. However, for the FAST main reflector, the image block near the nodes have high similarity, and it will be difficult to perform node matching by traditional methods.

Move the camera to shoot 2D images of the same target area and the camera move distance can be ignored relative to the shooting distance. The images captured at different positions are approximately considered to have a 2D-2D projective transformation, which is described by a homography matrix. Suppose we have two images I_1, I_2, point $P = (x, y, 1)$ in I_1 and its corresponding point in I_2 is $Q = (x', y', 1)$ and with homogeneous representation of two points, we have:

$$\lambda Q = \lambda \begin{bmatrix} x' \\ y' \\ 1 \end{bmatrix} = \boldsymbol{H} \begin{bmatrix} x \\ y \\ 1 \end{bmatrix} = \begin{bmatrix} h_0 & h_1 & h_2 \\ h_3 & h_4 & h_5 \\ h_6 & h_7 & h_8 \end{bmatrix} \begin{bmatrix} x \\ y \\ 1 \end{bmatrix} = \boldsymbol{H} P \tag{5}$$

where λ is the arbitrary scale factor. $\boldsymbol{H}$ is the homography matrix between I_1 and I_2. Let $h_8 = 1$ to eliminate the scale factor, Equation (5) can be transformed into two linear equation:

$$\begin{aligned} x' &= \frac{h_0 x + h_1 y + h_2}{h_6 x + h_7 y + 1} \\ y' &= \frac{h_3 x + h_4 y + h_5}{h_6 x + h_7 y + 1} \end{aligned} \tag{6}$$

there are eight unknowns in Equation (6), a pair of points can determine two linear equations, so at least four pairs of points are required to solve all the parameters of $\boldsymbol{H}$.

In the FAST main reflector image as shown in Figure 1(a), there is a salient feature in the image. By detecting this feature, the node closest to the feature in different images can be matched and this is the only matching node pair that can be determined. In order to recover $\boldsymbol{H}$, three corresponding node pairs need to be determined, which can be processed by the following method.

Suppose P, Q are matching nodes in I_1, I_2 respectively; the six nodes in I_1 closest to P is $\Phi = \{P_i, i = 1, 2, \cdots, 6\}$. Similarly in I_2 the six nodes closest to Q are $\Psi = \{Q_i, i = 1, 2, \cdots, 6\}$. Randomly select three nodes in Φ plus P consists of four nodes in I_1 : $\phi = \{P, P_1, P_2, P_3\}$ and the node corresponding to P in I_2 is Q, however there must be a one to one correspondence between the three nodes in Ψ plus Q and the nodes in ϕ, where there are 120 possible permutations. Traverse 120 possible permutations, compute $\boldsymbol{H}$ by Equation (6) and calculate the number of matching nodes by $\boldsymbol{H}$. The $\boldsymbol{H}$ with the most matching points is the correct homography matrix between the two images. Finally, all nodes in the two images are matched by correct $\boldsymbol{H}$.

4 3D RECONSTRUCTION

In this section, the camera model and distortion model used in this paper will be introduced, meanwhile triangulation and the bundle adjustment algorithm will be adopted for 3D reconstruction.

4.1 Camera Model

In this paper, we use the pinhole camera model, a 3D point $M = (X_w, Y_w, Z_w)$ in the world coordinate system project to the image plane then the transformation into the pixel coordinate system is $m = (u, v)$ and the relationship between M and m is as follows:

$$\begin{aligned} s \begin{bmatrix} u \\ v \\ 1 \end{bmatrix} &= \begin{bmatrix} \frac{1}{d_x} & \gamma & u_0 \\ 0 & \frac{1}{d_y} & v_0 \\ 0 & 0 & 1 \end{bmatrix} \begin{bmatrix} f & 0 & 0 & 0 \\ 0 & f & 0 & 0 \\ 0 & 0 & 1 & 0 \end{bmatrix} \begin{bmatrix} \boldsymbol{R} & \boldsymbol{T} \\ \boldsymbol{0}^T & 1 \end{bmatrix} \begin{bmatrix} X_w \\ Y_w \\ Z_w \\ 1 \end{bmatrix} \\ &= \begin{bmatrix} f_x & \gamma & u_0 & 0 \\ 0 & f_y & v_0 & 0 \\ 0 & 0 & 1 & 0 \end{bmatrix} \begin{bmatrix} \boldsymbol{R} & \boldsymbol{T} \\ \boldsymbol{0}^T & 1 \end{bmatrix} \begin{bmatrix} X_w \\ Y_w \\ Z_w \\ 1 \end{bmatrix} \end{aligned} \tag{7}$$

where s is the arbitrary scale factor, d_x and d_y is the physical size of each pixel in the x axis and y axis, f is focal length, γ is the tilt factor, and (u_0, v_0) is the principal point of the pixel coordinate system. $\boldsymbol{R}$ is a 3×3 rotation matrix and $\boldsymbol{T} = [t_x, t_y, t_z]^T$ is a translation vector that represents the origin coordinates of the world coordinate system in the camera coordinate system.

As a result of several types of imperfections in the design and assembly of lenses composing the camera optical system (Weng & Cohen 1992), several types of distortion would occur inevitably under actual circumstances, which can be written as:

$$\begin{aligned} u' &= u + \delta_x(x, y) f_x \\ v' &= v + \delta_y(x, y) f_y \end{aligned} \tag{8}$$

where (u', v') is the real observed pixel image coordinates, (u, v) is ideal pixel image coordinates, δ_x, δ_y represent the distortion along the x-axis direction and y-axis direction on the normalized image plane respectively. According to the different distortion directions, the distortion is divided into radial distortion, tangential distortion and thin prism

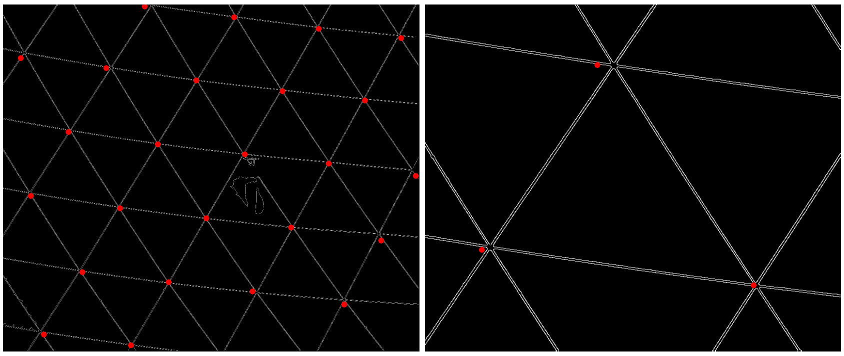

(a) (b)

Fig. 4 (a) Rough detection result. (b) A partial enlarged view.

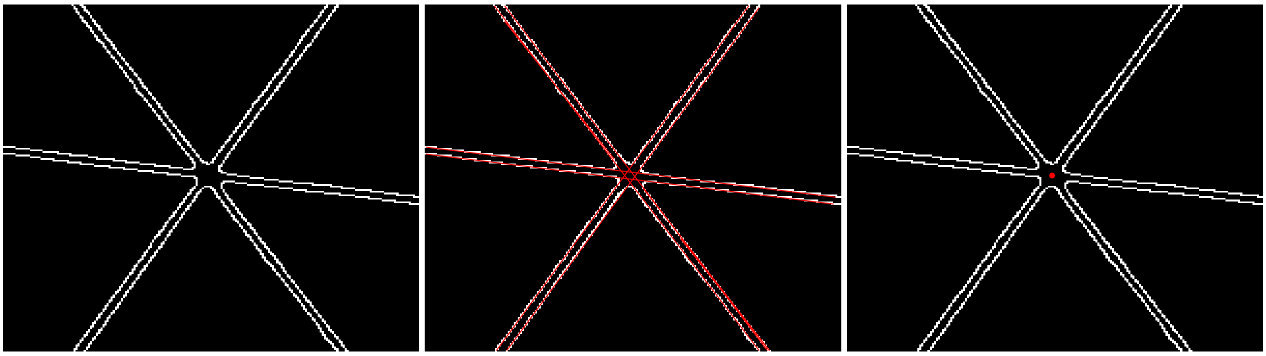

(a) (b) (c)

Fig. 5 (a) ROI. (b) Lines detect in (a). (c) Nodes detect in (a).

distortion (Heikkila & Silven 1997; Wang et al. 2008). In most cases, the radial distortion of the camera is dominant (Zhang 2000), in this paper, we only consider the first two-order radial distortion.

$$\begin{aligned} \delta_x(x,y) &= x(k_1(x^2+y^2)+k_2(x^2+y^2)^2) \\ \delta_x(x,y) &= y(k_1(x^2+y^2)+k_2(x^2+y^2)^2) \end{aligned} \tag{9}$$

k_1, k_2 represent the first-order radial distortion coefficient and the second-order radial distortion coefficient respectively. (x, y) represents the coordinates on the normalized image plane.

$$\begin{aligned} x &= \frac{u-u_0}{f_x} \\ y &= \frac{v-v_0}{f_y} \end{aligned} \tag{10}$$

4.2 Triangulation and Bundle Adjustment

Rewrite the projection Equation (7):

$$s\tilde{m} = s\begin{bmatrix} u \\ v \\ 1 \end{bmatrix} = \boldsymbol{K}[\boldsymbol{R},\boldsymbol{T}]\begin{bmatrix} X_w \\ Y_w \\ Z_w \\ 1 \end{bmatrix} = \boldsymbol{P}\begin{bmatrix} X_w \\ Y_w \\ Z_w \\ 1 \end{bmatrix} = \boldsymbol{P}\tilde{M} \tag{11}$$

where $\tilde{m} = [u, v, 1]^T$ and $\tilde{M} = [X_w, Y_w, Z_w, 1]^T$, which represent the homogeneous coordinates of the image point and the world point respectively. $\boldsymbol{P}$ represents the projection matrix, $\boldsymbol{K}$ is the intrinsic parameter matrix and $[\boldsymbol{R},\boldsymbol{T}]$ is the extrinsic parameter matrix.

$$\begin{aligned} \boldsymbol{K} &= \begin{bmatrix} f_x & \gamma & u_0 \\ 0 & f_y & v_0 \\ 0 & 0 & 1 \end{bmatrix} \\ [\boldsymbol{R},\boldsymbol{T}] &= \begin{bmatrix} r_{11} & r_{12} & r_{13} & t_x \\ r_{21} & r_{22} & r_{23} & t_y \\ r_{31} & r_{32} & r_{33} & t_z \end{bmatrix} \end{aligned} \tag{12}$$

Equation (11) cross product $\tilde{m}$ both sides:

$$\tilde{m} \times (\boldsymbol{P}\tilde{M}) = \boldsymbol{0} \tag{13}$$

expand Equation (13):

$$\begin{aligned} u(\boldsymbol{P}_3\tilde{M}) - \boldsymbol{P}_1\tilde{M} &= 0 \\ v(\boldsymbol{P}_3\tilde{M}) - \boldsymbol{P}_2\tilde{M} &= 0 \\ u(\boldsymbol{P}_2\tilde{M}) - v(\boldsymbol{P}_1\tilde{M}) &= 0 \end{aligned} \tag{14}$$

where $\boldsymbol{P}_i$ is the i^{th} row of the projection matrix $\boldsymbol{P}$. The third equation can be obtained by the first and second

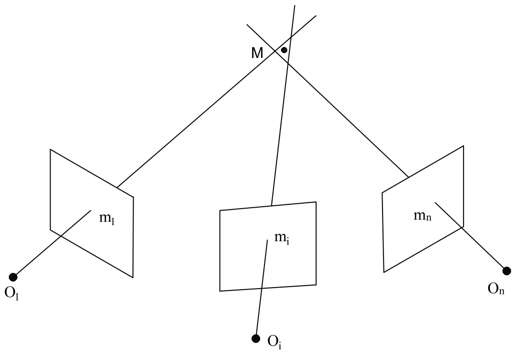

Fig. 6 Triangulation Algorithm.

equations, so there are only two independent equations:

$$\begin{bmatrix} u\boldsymbol{P}_3 - \boldsymbol{P}_1 \\ v\boldsymbol{P}_3 - \boldsymbol{P}_2 \end{bmatrix} \tilde{M} = 0 \tag{15}$$

$\tilde{M}$ has three unknowns, but Equation (15) can only provide two equations, indicating that the reconstruction of a 3D point requires at least two positions to shoot the target point to obtain a solution in the sense of least squares. In order to enhance the robustness, the target is generally shot in multiple directions, as shown in Figure 6. Assuming that a target is shot in N directions, $2N$ equations can be obtained:

$$\boldsymbol{A}\tilde{M} = \boldsymbol{0}, \boldsymbol{A} = \begin{bmatrix} u_1\boldsymbol{P}_{13} - \boldsymbol{P}_{11} \\ v_1\boldsymbol{P}_{13} - \boldsymbol{P}_{12} \\ \cdots \\ u_i\boldsymbol{P}_{i3} - \boldsymbol{P}_{i1} \\ v_i\boldsymbol{P}_{i3} - \boldsymbol{P}_{i2} \\ \cdots \\ u_N\boldsymbol{P}_{N3} - \boldsymbol{P}_{N1} \\ v_N\boldsymbol{P}_{N3} - \boldsymbol{P}_{N2} \end{bmatrix} \tag{16}$$

(u_i, v_i) represents the image coordinates corresponding to the i^{th} position of M, and $\boldsymbol{P}_{ij}$ represents the j^{th} row of the i^{th} projection matrix.

The projection matrix $\boldsymbol{P} = \boldsymbol{K}[\boldsymbol{R}, \boldsymbol{T}]$, where $\boldsymbol{K}$ is the intrinsic parameter matrix and it will not change as the camera moves, but $[\boldsymbol{R}, \boldsymbol{T}]$ represents the position information of the camera coordinate system relative to the world coordinate system, which is in contrast. Since we do not know any 3D information, it can be assumed that the world coordinate system coincides with the first position camera coordinate system. According to the knowledge of multi-view geometry (Hartley & Zisserman 2004), $[\boldsymbol{R}_i, \boldsymbol{T}_i]$ of the i^{th} position can be obtained by the essential matrix between two images. Once we obtain $[\boldsymbol{R}, \boldsymbol{T}]$ of all locations, use Equation (16) for 3D reconstruction.

Due to data noise, node extraction accuracy and camera distortion, etc., the 3D points contain certain errors. To improve accuracy, apply the bundle adjustment algorithm to optimize them. Suppose that a camera is used to shoot images at m locations, and the field of view

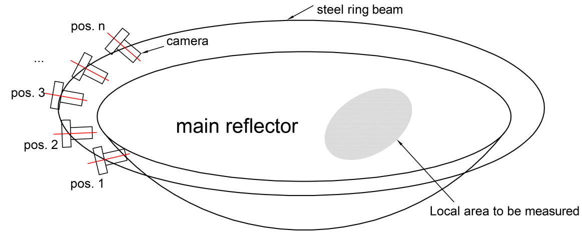

Fig. 7 Schematic diagram of measurement site.

contains n nodes. Due to the limitation of the camera field of view, the camera cannot shoot n nodes in a single position. Use the nonlinear least squares optimization algorithm to optimize Equation (17):

$$G(\boldsymbol{\phi}) = \frac{1}{2}\sum_{i=1}^{n}\sum_{j=1}^{m}\delta_{ij}\|\hat{u}_{ij} - u_{ij}(\boldsymbol{C}_j, M_i)\| = \frac{1}{2}\sum_{i=1}^{n}\sum_{j=1}^{m}\delta_{ij}e_{ij} \tag{17}$$

where $\boldsymbol{\phi} = (\boldsymbol{C}_1, \boldsymbol{C}_2 \cdots, \boldsymbol{C}_m, M_1, M_2, \cdots, M_n)$ are the parameters need to be estimated. $\boldsymbol{C}_j = (f, k_1, k_2, u_0, v_0, \gamma, \boldsymbol{R}_j, \boldsymbol{T_j})$ is camera parameters at j^{th} position, intrinsic parameters are constant in different position, $\boldsymbol{R}_j$ is represented by three Euler angles, $\boldsymbol{T}_j$ and M_i are represented by three parameters respectively. Thus $\boldsymbol{\phi} \in \mathbb{R}^{6+6m+3n}$. $\hat{u}_{ij}$ represents the image coordinates of the i^{th} point observed by the camera at the j^{th} position. u_{ij} represents the image coordinates obtained by projecting the i^{th} point at the j^{th} camera position. If the i^{th} point is visible at the j^{th} position of the camera $\delta_{ij} = 1$, otherwise $\delta_{ij} = 0$. This is a high-dimensional nonlinear optimization problem, using the Levenberg-Marquardt algorithm to solve it and it is essential to provide a good initial value. The initial values of the parameters in this paper are given according to the following rules:

1. Focal length and pixel physical: f, d_x, d_y are provided by the camera manufacturer.
2. Principal point: (u_0, v_0) is the image center coordinates.
3. Distortion parameters: k_1, k_2 set to zero.
4. Extrinsic parameters: $\boldsymbol{R}_i, \boldsymbol{T}_i$ obtained by essential matrix.
5. 3D point: M_j use the triangulation algorithm.

5 EXPERIMENT

In order to verify the effectiveness and accuracy of the proposed algorithm, the actual measurement experiments are conducted. At the FAST site, a camera is used to capture a series of images of a certain area of the FAST main reflector as shown in Figure 7, and the image resolution is 2452 × 2056. Apply the algorithm proposed in this paper to perform node detection and node matching on the image respectively. Then the matched nodes are used to perform the 3D reconstruction of the FAST nodes.

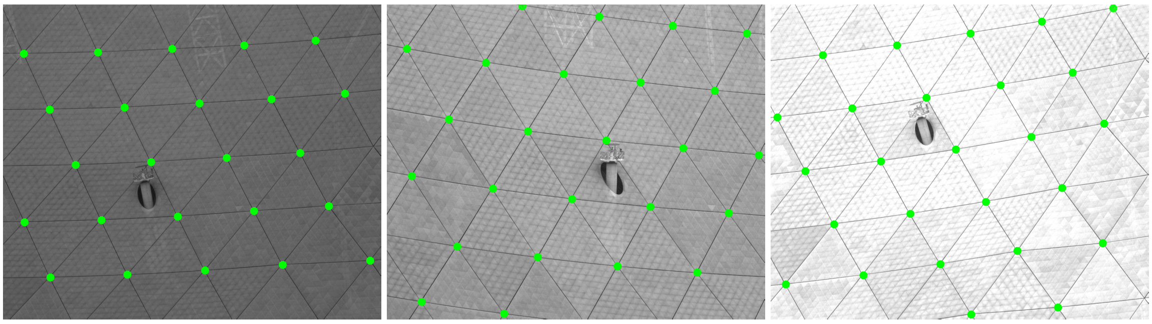

(a) (b) (c)

Fig. 8 Node detection result under different conditions. (a) The result in dark lighting conditions. (b) The result in medium lighting conditions. (c) The result in bright lighting conditions.

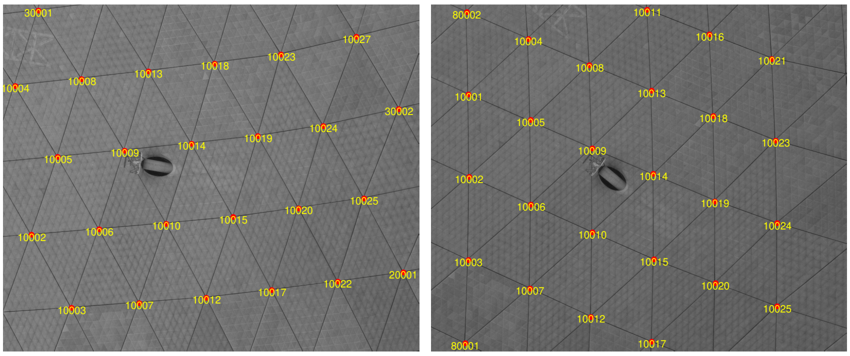

Fig. 9 Node matching result.

5.1 Node Detection and Matching Experiment

The FAST is located in the mountainous area of Guizhou, where the climatic conditions and lighting conditions are unstable. In order to evaluate the stability of the node detection algorithm, the node detection process is performed on the images under three lighting conditions. The detection result under dark lighting conditions as shown in Figure 8(a), medium lighting conditions as shown in Figure 8(b), and bright lighting conditions as shown in Figure 8(c). It indicates that for different lighting conditions, the node detection algorithm has high adaptability. We test a set of 20 images and the average recognition rate can reach 97%, which satisfies the measurement demand.

The camera captures a set of 20 images and the node data are collected through node detection, then we apply the algorithm proposed in this paper to perform node matching. Randomly select two images and the matching result as shown in Figure 9. In order to eliminate the singularity of node coding, the sequence number of the node in the image is coded according to the image sequence number of its first appearance. For example, the node code 80001 means that the node appears for the first time in the 8th image. It is noted that we assume the nodes in two adjacent images have the largest matching number, so it is required that the two adjacent images have a larger overlap area when capturing images. If the overlap area is small, it may cause matching error. Generally, the overlap area is approximately 2/3 image size.

5.2 3D Reconstruction Experiment and Accuracy Analysis

The position of the nodes was adjusted to deform a local area of the FAST main reflector into a sphere with a radius of 300 m. A CCD camera was used to collect a set of 62 images from various directions, and there are about 19 nodes in each image. After node detection and matching for each image, a 3D reconstruction process can be performed. The CCD camera parameters used are as follows: focal length $f = 75$ mm; pixel physical size $d_x = d_y = 3.45\,\mu$m; and image principal point coordinates $(u_0, v_0) = (1226, 1028)$. The 3D reconstruction result is shown in Table 1.

In order to evaluate the accuracy of 3D reconstruction, the reconstructed 3D points are used for spherical fitting. In the experiment, the radius of the target area $R = 300$ m, so the spherical surface contains three unknown parameters, which are the sphere center coordinates (x_0, y_0, z_0), using the nonlinear least squares algorithm performs spherical fitting. Suppose the number of reconstructed 3D points is

Table 1 Reconstructed 3D Point Coordinates

No.	X(m)	Y(m)	Z(m)	No.	X(m)	Y(m)	Z(m)
1	29.7565	–4.0037	–2.7365	10	–19.9299	–11.7502	9.0734
2	9.7978	–10.6877	2.4813	11	9.8483	8.5515	–5.7213
3	–0.0427	–13.7849	5.5886	12	–0.0209	5.3336	–2.8782
4	–10.0871	–18.2594	9.9382	13	–19.4903	–0.6467	3.8736
5	19.7518	2.1659	–4.4629	14	–29.6038	–5.0308	8.6739
6	9.809	–1.1162	–1.7929	15	9.9196	18.3297	–9.3242
7	–0.0338	–4.2955	1.2025	16	0.0227	15.0781	–6.6126
8	–9.8292	–7.3734	4.5328	17	–9.8812	11.8482	–3.5509
9	19.895	11.9665	–8.2212	18	–19.4933	8.9681	–0.0751

n, and the residual corresponding to the i^{th} point is defined as:

$$\delta_i = (x_i - x_0)^2 + (y_i - y_0)^2 + (z_i - z_0)^2 - R^2 \quad (18)$$

where (x_i, y_i, z_i) is the reconstructed 3D coordinates of the i^{th} point, (x_0, y_0, z_0) is the parameters need to be estimated. Minimize the residual sum of square Equation (19) to get the sphere center coordinates.

$$(x_0, y_0, z_0) = argmin \sum_{i=1}^{n} \delta_i^2 \quad (19)$$

Computer the distance from each 3D reconstruct point to the sphere:

$$d_i = |\sqrt{(x_i - x_0)^2 + (y_i - y_0)^2 + (z_i - z_0)^2} - R| \quad (20)$$

Use the average distance from all 3D reconstruct points to the sphere to evaluate the reconstruction accuracy:

$$d = \frac{1}{n} \sum_{i=1}^{n} |d_i| \quad (21)$$

In this experiment, the number of reconstructed 3D points is $n = 18$. Using the radius-constrained spherical fitting method to find the average distance from all points to the sphere is $d = 12.299$mm, satisfying the preliminary measurement needs.

6 CONCLUSIONS

This paper applies photogrammetry to measure the surface shape of the FAST main reflector. Nodes are extracted as image information through their natural feature, without the demand for sticking the cooperation target on the reflective surface. It is a less manual intervention, a fast and convenient method without any impact on the reflector. We propose a two-step method to detect nodes, first approximately locating the position and second crop ROI for precise detection. We tested a series of pictures, under normal lighting conditions, and the recognition rate was about 97%. Then, we applied the node combination method to recover the homography matrix between two images for node matching. Triangulation and bundle adjustment algorithms are adopted to reconstruct the 3D points. In the experiment, result shows that the measurement accuracy of the sphere with a radius of 300 m is 12.299 mm. This paper mainly measures a local area of the FAST reflector and reconstructs a small number of nodes. In future work, it is possible to apply the photogrammetric method to measure the entire reflector.

References

Canny, J. 1986, IEEE Transactions on Pattern Analysis and Machine Intelligence, 8, 679

Ching, Y. T. 2001, Pattern Recognition Letters, 22, 421

Edmundson, K., & Baker, L. 2001, in 17th Annual Coordinate Measurement Systems Committee Conference, 1

Hall, R., Goldman, M. A., Parker, D. H., & Payne, J. M. 1998, in Society of Photo-Optical Instrumentation Engineers (SPIE) Conference Series, 3357, Advanced Technology MMW, Radio, and Terahertz Telescopes, ed. T. G. Phillips, 265

Hartley, R., & Zisserman, A. 2004, Multiple View Geometry in Computer Vision/2nd ed (Cambridge Univ. Press)

Heikkila, J., & Silven, O. 1997, in Proceedings of IEEE Computer Society Conference on Computer Vision and Pattern Recognition, 1106

KaLviainen, H., & Hirvonen, P. 1997, Pattern Recognition Letters, 18, 77

Li, D., & Pan, Z. 2016, Radio Science, 51, 1060

Morison, I. 2007, Astronomy and Geophysics, 48, 5.23

Nan, R. 2006, Science in China: Physics, Mechanics and Astronomy, 49, 129

Nan, R., & Li, H. 2014, entia Sinica (Physica, Mechanica & Astronomica), 44, 1063

Ruze, J. 1966, IEEE Proceedings, 54, 633

Subrahmanyan, R. 2005, IEEE Transactions on Antennas and Propagation, 53, 2590

Tang, W., Zhu, L.-C., & Wang, Q.-M. 2020, RAA (Research in Astronomy and Astrophysics), 20, 126

Wang, J., Shi, F., Zhang, J., & Liu, Y. 2008, Pattern Recognition, 41, 607

Weng, J., & Cohen, P. 1992, IEEE Transactions on Pattern Analysis & Machine Intelligence, 14, 965

Wielebinski, R., Junkes, N., & Grahl, B. H. 2011, Journal of Astronomical History and Heritage, 14, 3

Xu, L., Oja, E., & Kultanen, P. 1990, Pattern Recognition Letters, 11, 331

Zhang, Z. 2000, IEEE Transactions on Pattern Analysis and Machine Intelligence, 22, 1330

Zhou, J., Zhou, Q., Liu, J., Xu, D., & Shu, L. 2010, in Society of Photo-Optical Instrumentation Engineers (SPIE) Conference Series, 7656, 5th International Symposium on Advanced Optical Manufacturing and Testing Technologies: Optical Test and Measurement Technology and Equipment, eds. Y. Zhang, J. Sasián, L. Xiang, & S. To, 76561V